

MR-Based PET Attenuation Correction using a Combined Ultrashort Echo Time/Multi-Echo Dixon Acquisition

Paul Kyu Han^{1,2,†}, Debra E. Horng^{1,2,†}, Kuang Gong^{1,2}, Yoann Petibon^{1,2}, Kyungsang Kim^{1,2},
Quanzheng Li^{1,2}, Keith A. Johnson^{1,2,3,4}, Georges El Fakhri^{1,2}, Jinsong Ouyang^{1,2},
and Chao Ma^{1,2*}

¹Gordon Center for Medical Imaging, Department of Radiology, Massachusetts General Hospital, Boston, MA 02114

²Department of Radiology, Harvard Medical School, Boston, MA 02115

³Department of Neurology, Massachusetts General Hospital, Boston, MA 02114

⁴Center for Alzheimer Research and Treatment, Department of Neurology, Brigham and Women's Hospital, Boston, MA 02115

Running Title: MR-Based PET AC using mUTE

*Correspondence to: Chao Ma, PhD
Gordon Center for Medical Imaging
Massachusetts General Hospital
125 Nashua Street, Suite 660
Boston, MA, 02114
Telephone: +1-617-643-1961
E-mail: cma5@mg.harvard.edu

†These authors contributed equally to this work.

Abstract

Purpose: To develop a magnetic resonance (MR)-based method for estimation of continuous linear attenuation coefficients (LAC) in positron emission tomography (PET) using a physical compartmental model and ultrashort echo time (UTE)/multi-echo Dixon (mUTE) acquisitions.

Methods: We propose a three-dimensional (3D) mUTE sequence to acquire signals from water, fat, and short- T_2 components (e.g., bones) simultaneously in a single acquisition. The proposed mUTE sequence integrates 3D UTE with multi-echo Dixon acquisitions and uses sparse radial trajectories to accelerate imaging speed. Errors in the radial k-space trajectories are measured using a special k-space trajectory mapping sequence and corrected for image reconstruction. A physical compartmental model is used to fit the measured multi-echo MR signals to obtain fractions of water, fat and bone components for each voxel, which are then used to estimate the continuous LAC map for PET attenuation correction.

Results: The performance of the proposed method was evaluated via phantom and in vivo human studies, using LACs from Computed Tomography (CT) as reference. Compared to Dixon- and atlas-based MRAC methods, the proposed method yielded PET images with higher correlation and similarity in relation to the reference. The relative absolute errors of PET activity values reconstructed by the proposed method were below 5% in all of the four lobes (frontal, temporal, parietal, occipital), cerebellum, whole white matter and gray matter regions across all subjects (n=6).

Conclusions: The proposed mUTE method can generate subject-specific, continuous LAC map for PET attenuation correction in PET/MR.

Keywords: PET attenuation correction; MR-based attenuation correction; MRAC; ultrashort echo time (UTE); multi-echo Dixon; PET/MR; continuous LAC;

Introduction

Position emission tomography (PET) / magnetic resonance imaging (MRI) is an emerging imaging modality that shows great potential in clinical applications. PET/MR allows high-resolution anatomical imaging with excellent soft-tissue contrast as well as functional and molecular information. PET/MR also provides unique opportunities for improving the quality of PET imaging via incorporating motion field and anatomical prior information from MR into PET image reconstruction¹⁻³. Furthermore, combining PET and MR in a single imaging session enables estimation of physiological processes that otherwise would be impossible with PET or MR alone⁴.

Despite the usefulness and growing interest of PET/MR imaging, PET attenuation correction with MR is not a trivial task. MR signal is a complex function of many variables such as proton density and relaxation times but not the electron density, which determines the linear attenuation coefficients (LAC) of different tissues. This fundamental lack of information makes PET attenuation correction with MR difficult. The issue becomes obvious in tissues such as bone, which displays high LAC due to the high electron density but low MR signal due to the very short T_2 decay and low proton density.

Various MR-based attenuation correction (MRAC) methods have been developed to address this issue^{5,6}. Early developments used MR images to segment/classify voxels into different tissue classes and then assigned a specific LAC value to each class for PET attenuation correction. The MRAC method implemented in the first generation of commercial PET/MR scanners segments the imaging object into 3-tissue (i.e., air, soft-tissue, and lung)⁷ or 4-tissue classes (i.e., air, fat, non-fat soft-tissue, and lung)^{8,9} based on T_1 -weighted or two-point Dixon MR images. Methods employing ultrashort echo time (UTE) or zero echo time (ZTE) acquisitions have also been developed to detect bone signal and assign a single LAC to bone tissue¹⁰⁻¹⁴. However, these early methods do not properly account for continuous variations in LAC and suffer from biases in the resultant PET reconstructions¹⁵.

Several MRAC methods have been developed to estimate LAC maps with continuous distribution. One family of methods exploit a pre-compiled template (i.e., atlas) generated from Computed Tomography (CT)-MR databases and employ image registration to align acquired MR images with the template and get LAC maps with continuous distribution. A partial list of these methods include deformable registration methods^{16,17} with evaluation of morphologic similarity¹⁸,

machine learning approaches such as Gaussian process regression^{16,19}, Gaussian mixture regression model²⁰, support vector regression model²¹, structured random forest²², and patch-based approaches exploiting local subregions of images rather than the whole image²³⁻²⁶. Recently, tissue segmentation information has also been proposed for improved estimation of LAC²⁷⁻³¹. Although these atlas-based MRAC methods work well in general for brain imaging of subjects with normal anatomy, these methods are known to be sensitive to registration errors, cannot account for inter-subject variability, and cannot properly handle subject-specific anatomical abnormality that differs from the template.

Another family of methods estimate LAC maps with continuous distribution by modeling the relationship between MR and CT information. Methods employing ZTE acquisition have been developed to model the relationship between ZTE signal intensities and CT Hounsfield values to obtain pseudo-CT images with continuous distribution of bone³¹⁻³⁵. Methods employing UTE acquisition have been developed to model the relationship between relaxation time (e.g., R_2^*) information and CT Hounsfield values^{36,37} or LAC³⁸ to obtain pseudo-CT images or LAC maps with continuous distribution. However, these methods rely on empirical relationship derived from MR and CT images, and require MR and CT dataset pairs to establish the relationship.

Recently, deep neural networks (DNN) have also been proposed for MRAC to generate LAC maps with continuous distribution. Algorithms based on feed forward neural network (FFNN)³⁹, general adversarial network (GAN)^{40,41}, and convolutional neural network (CNN) with convolutional auto encoder (CAE)^{14,42} or U-net structure⁴³⁻⁴⁶ with group convolution modules⁴⁷ have shown encouraging results in generating subject-specific LAC maps with continuous distribution. These methods generate pseudo-CT images directly from conventional MR images (e.g., Dixon or T₁-weighted images) which are later converted to LAC maps through bilinear transformation. Though promising, one major drawback of these methods is in the requirement of substantial number of MR and CT dataset pairs to train and generate LAC maps, which may not be easily available for specific applications, e.g., oncologic applications.

In this work, we propose a new physical model-based MRAC method to estimate subject-specific LAC maps with continuous distribution. More specifically, we propose a combined UTE/multi-echo Dixon (mUTE) sequence along with a physical compartmental model to estimate the different proportions of water, fat and bone components in each voxel, which are subsequently

used to estimate LAC with continuous distribution. The proposed method (i) allows to estimate continuous LAC directly from MR through physical compartmental modeling, (ii) does not require any training datasets to model relationships or to generate subject-specific LAC maps, (iii) provides robust fat-water separation that does not require registration by performing UTE and multi-echo Dixon in a single acquisition, and (iv) is not mutually exclusive to other MRAC methods. The feasibility of the proposed method is demonstrated via a phantom experiment with pig tibia and in vivo experiments with 6 subjects (1 patient with mild-cognitive impairment and 5 cognitively healthy volunteers) undergoing brain MR and PET/CT examinations using ^{11}C -Pittsburgh compound B (PiB). Potential usefulness of the proposed method and limitations of the current work are also discussed.

Materials and Methods

A Physical Compartmental Model for Continuous LAC

The proposed work is based on a physical compartmental model to estimate LAC using MR. A single imaging voxel is assumed to consist of water, fat, bone and air compartments, with different proportions of each of the compartments. The LAC at a single voxel (μ_{voxel}) can be defined as:

$$\mu_{\text{voxel}} = p_W \cdot \mu_W + p_F \cdot \mu_F + p_B \cdot \mu_B \quad [1]$$

where p_W , p_F , and p_B each denote the volume fractions of water, fat and bone, respectively, and μ_W , μ_F , and μ_B each denote the LAC of water, fat, and bone, respectively. Note that the LAC of air is negligible and therefore ignored in Eq. 1. In this model, water and fat refer to those not only within soft-tissue but also the long-T₂ components of water and fat within the bone, respectively. The advantage of this physical compartmental model is estimation of the continuous variations of LAC via the fraction of the compartments, which can be estimated with MR using the strategy proposed thereafter.

Proposed 3D mUTE Sequence

Our proposed three-dimensional (3D) mUTE sequence combines 3D UTE⁴⁸ and multi-echo Dixon imaging^{49,50} in a single acquisition (Fig. 1). Multi-echo radial images are acquired at

different TE times every other repetition time (TR). The following signal model is used to estimate the proton densities of water, fat, and bone from the acquired multi-echo images:

$$S(TE_j) = \begin{cases} (\rho_B + (\rho_W + \rho_F \cdot g(TE_j)) \cdot e^{-R_2^* TE_j}) \cdot e^{i \cdot 2\pi \cdot \Delta f_{B0} \cdot TE_j} & \text{for } j = 1 \\ (\rho_W + \rho_F \cdot g(TE_j)) \cdot e^{-R_2^* TE_j} \cdot e^{i \cdot 2\pi \cdot \Delta f_{B0} \cdot TE_j} & \text{for } j = 2, \dots, J \end{cases} \quad [2]$$

where $S(TE_j)$ denotes the signal at a single imaging voxel acquired at the j^{th} TE time (TE_j); ρ_W , ρ_F , and ρ_B each denote the proton densities of water, fat, and bone, respectively; $g(t_j) = \sum_{m=1}^M \alpha_m \cdot e^{i \cdot 2\pi \cdot (\Delta f_{fat,m}) \cdot t_j}$ denotes the M -peak (i.e., $M = 6$) spectral model of fat with relative amplitude α_m (i.e., $\sum_{m=1}^M \alpha_m = 1$) and frequency offset $\Delta f_{fat,m}$, where α_m and $\Delta f_{fat,m}$ are known from the literature^{51,52}; $R_2^* = 1/T_2^*$ denotes the single representative relaxation rate of both water and fat⁵³; and Δf_{B0} denotes the frequency offset due to magnetic field inhomogeneity (B_0). Note that we assume that the signal from bone only exists in the signal model for the UTE image (i.e., $j = 1$) because of the short T_2^* of bone tissue. The signal model in Eq. 2 has in total five unknowns, i.e., ρ_W , ρ_F , ρ_B , R_2^* and Δf_{B0} , which requires at least five different TEs for estimation. In our current implementation, we acquire MR signals at seven different TEs in every two TRs (i.e., one UTE and six multi-echo Dixon acquisitions for robust fat-water separation⁵⁴) for more robust parameter estimation. The volume fractions of water, fat, and bone compartments in Eq. 1 can be determined by using the estimated proton densities as follows:

$$p_W = \frac{V_W}{V_W + V_F + V_B} = \frac{\frac{\rho_W}{c_W}}{\frac{\rho_W}{c_W} + \frac{\rho_F}{c_F} + \frac{\rho_B}{c_B}} \quad [3]$$

$$p_F = \frac{V_F}{V_W + V_F + V_B} = \frac{\frac{\rho_F}{c_F}}{\frac{\rho_W}{c_W} + \frac{\rho_F}{c_F} + \frac{\rho_B}{c_B}} \quad [4]$$

$$p_B = \frac{V_B}{V_W + V_F + V_B} = \frac{\frac{\rho_B}{c_B}}{\frac{\rho_W}{c_W} + \frac{\rho_F}{c_F} + \frac{\rho_B}{c_B}} \quad [5]$$

where V_W , V_F , and V_B each denote the volume occupied by water, fat, and bone within a voxel, respectively, and c_W , c_F , and c_B each denote the proton concentration of water, fat, and bone, respectively.

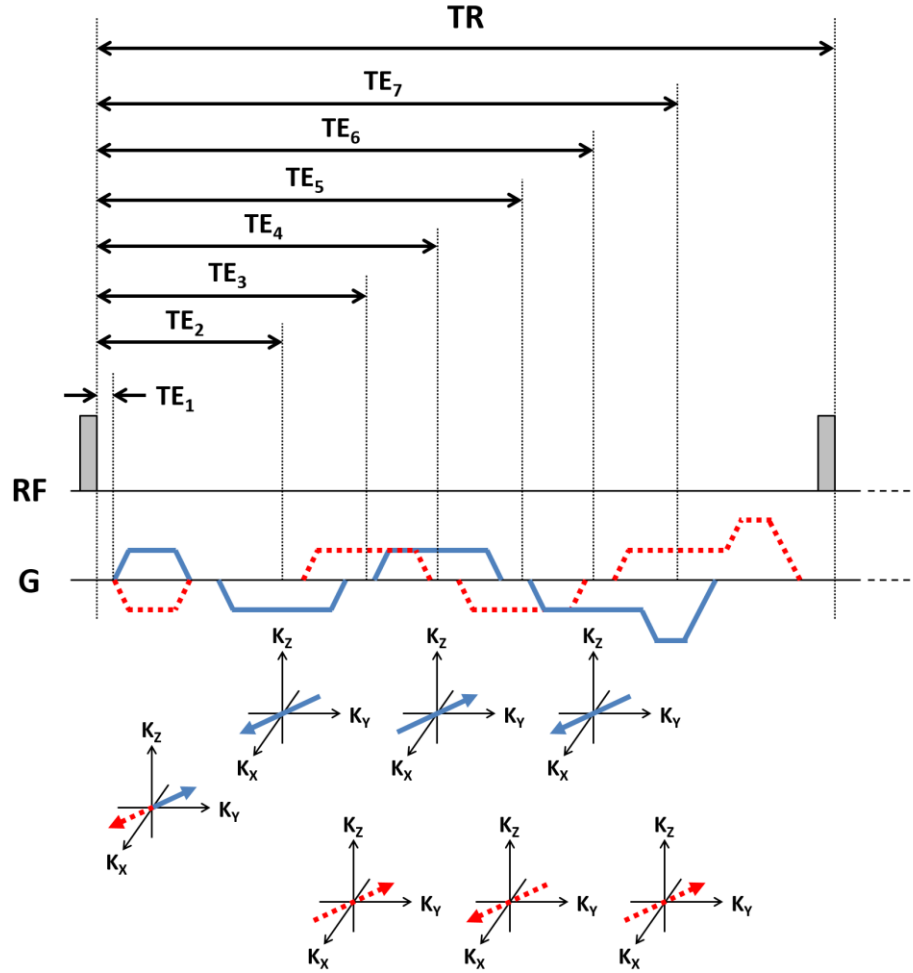


Figure 1. Pulse sequence diagram of the proposed mUTE sequence. The proposed mUTE sequence consists of UTE and multi-echo radial images, with alternating acquisition of multi-echo images at different TE times every other TR. Acquisitions from odd TR (e.g., TE₁, TE₃, TE₅, TE₇, labeled in red dashed line) and even TR (e.g., TE₂, TE₄, TE₆, labeled in blue solid line) are shown with a schematic diagram representing the k-space trajectory traversed by each readout gradients. Notice that this interleaved acquisition scheme allows the same k-space coverage of spokes for all images.

Phantom Experiment

A phantom was made by placing a pig tibia containing muscle, fat, and bone inside a plastic container. The container was then filled with 5% gelatin mixture containing radioactive ^{18}F to resemble soft tissue, along with two plastic spheres containing different concentrations of radioactive ^{18}F to help visualize the location of pig tibia. The phantom was then imaged using a whole-body PET/MR scanner (Biograph mMR, software version VB20P, Siemens Healthcare, Erlangen, Germany). PET imaging was performed for 15 min. MR acquisition was performed using the proposed 3D mUTE sequence (Fig. 1) with the following imaging parameters: field-of-view (FOV) = $240 \times 240 \times 240 \text{ mm}^3$, resolution = $1.875 \times 1.875 \times 1.875 \text{ mm}^3$, TR = 9.9 ms, TE₁₋₇ = 70, 2110, 2810, 3550, 4250, 4990, 5690 μs , flip angle = 10° , hard pulse duration = 100 μs , gradient ramp time = 400 μs (gradient slew rate = 48.9 mT/m/ms), plateau gradient amplitude = 19.57 mT/m, dwell time = 2.5 μs , number of radial spokes for UTE/multi-echo images = 51472/25736, and acquisition time = 8.5 min. Retrospective down-sampling was performed to test the feasibility of the proposed method in the case of radial spokes for UTE/multi-echo images = 6434/3217 (corresponding to an acceleration factor of 8). Additional acquisitions were performed with magnetization-prepared rapid acquisition with gradient echo (MPRAGE) and the manufacturer's two-point Dixon-based MRAC sequence. The phantom was separately imaged using a whole-body CT scanner (Biograph 64, Siemens Healthcare, Erlangen, Germany), with the following parameters: tube peak voltage = 120 kVp, tube current time product = 30 mAs, in-plane resolution = $0.56 \times 0.56 \text{ mm}^2$, and slice-thickness = 1 mm.

In Vivo Experiment

Six volunteers (1 patient with mild-cognitive impairment and 5 cognitively healthy volunteers; 3 males and 3 females; 48-86 years old) were scanned under a study protocol approved by our local Institutional Review Board (IRB) for Harvard Aging Brain Study (HABS), which includes separate PET/CT and MR scans. Written informed consent was obtained from all subjects before study participation. MR acquisitions were performed on a 3T MR scanner (MAGNETOM Trio, Siemens Healthcare, Erlangen, Germany) using the proposed 3D mUTE sequence (Fig. 1) with the following imaging parameters: FOV = $240 \times 240 \times 240 \text{ mm}^3$, resolution = $1.875 \times 1.875 \times 1.875 \text{ mm}^3$, TR = 8.0 ms, TE₁₋₇ = 70, 2110, 2310, 3550, 3750, 4990, 5190 μs , flip angle = 15° , hard pulse

duration = 100 μ s, gradient ramp time = 400 μ s (gradient slew rate = 48.9 mT/m/ms), plateau gradient amplitude = 19.57 mT/m, dwell time = 2.5 μ s, number of radial spokes for UTE/multi-echo images = 6434/3217 (corresponding to acceleration factor of 8), and acquisition time = 52 s. An additional acquisition was performed with MPRAGE for comparison.

A separate PET/CT examination was performed for the same subjects on a whole-body PET/CT scanner (Discovery MI, GE Healthcare, Milwaukee, Wisconsin, USA). The imaging protocol of PET consisted of 15 mCi bolus injection of ^{11}C -PiB followed by a dynamic scan for 70 min. Only data from 40-50 min. post injection (i.e., secular equilibrium of ^{11}C -PiB) were evaluated in the current work. CT imaging was performed with tube peak voltage = 120 kVp, tube current time product = 30 mAs, in-plane resolution = $0.56 \times 0.56 \text{ mm}^2$, and slice-thickness = 1 mm.

Image Reconstruction and LAC Map Generation

In the current work, sparse-sampling was incorporated to accelerate data acquisition and make the total scan time of the proposed mUTE sequence feasible in less than a minute. Image reconstruction based on non-uniform fast Fourier transform (NUFFT)⁵⁵ and SENSE^{56,57} was performed for UTE and multi-echo radial images by solving the following optimization problem:

$$\arg \min_x \|\Omega(\mathcal{F}Sx) - y\|_2^2 + \lambda \|\Psi(x)\|_1 \quad [6]$$

where the first term denotes data consistency, the second term denotes l_1 -regularization penalty, x denotes the artifact-free image, Ω denotes the sampling matrix, \mathcal{F} denotes the spatial Fourier transform matrix, S denotes the coil sensitivity matrix, y denotes the under-sampled k-space measurement, λ denotes the regularization parameter, and Ψ denotes the sparsifying transform. Total variation⁵⁸ was used for Ψ and the optimization problem was solved using alternating minimization. The regularization parameter λ was chosen to be 10^{-3} of the maximum intensity of the original data, based on the data discrepancy principle⁵⁹. The k-space trajectories of the UTE and multi-echo radial acquisitions were measured and corrected in image reconstruction to reduce the effects of eddy currents on the resultant images (See Appendix for details).

Following image reconstruction, variable projection (VARPRO) algorithm⁶⁰ was used to estimate ρ_W , ρ_F , and ρ_B using Eq. 2. Subsequently, p_W , p_F , and p_B were estimated using Eqs. 3-

5, and the LAC was determined for each voxel using Eq. 1. The regions of air were determined via thresholding the UTE image, with an empirically determined threshold value: briefly, the UTE image was bias corrected⁶¹ and an air mask was generated via thresholding with a value determined by evaluating the signal intensity distribution of air^{14,32}. For the in vivo studies, an additional air support mask was generated by evaluating the frontal sinus region separately for improved delineation of air, similar to previous study³⁷. An additional bone support mask was also generated and applied for improved delineation of bone, via thresholding operation from a bone-enhanced image¹⁰. An LAC value of 0 cm^{-1} was assigned to voxels determined as air. The values μ_W of 0.099 cm^{-1} at 511 keV⁶² and c_W of 110.4 M^{63} were used in this study. Calibration of μ_F , μ_B , c_F and c_B was done by using CT-based attenuation maps at 511 keV from a representative in vivo subject dataset as the ground truth.

For the phantom study, an additional LAC map was generated from the manufacturer's two-point Dixon-based method for comparison. Then, PET images were reconstructed with attenuation correction using the LAC maps. The CT image was converted to LAC at 511 keV using bilinear transformation⁶⁴ and was registered to the PET imaging space via registration to MR image first and subsequently to PET using affine transformation (without shearing), prior to reconstruction. The ordered subset expectation maximization (OSEM) algorithm⁶⁵ was used with 3 iterations of 21 subsets to reconstruct PET images with the following parameters: image size = $344 \times 344 \times 127$, in-plane voxel size = $2.09 \times 2.09 \text{ mm}^2$, and slice-thickness = 2.03 mm.

For the in vivo study, additional LAC maps were generated using the two-point Dixon-based method⁸, an atlas-based method¹⁷, and the proposed mUTE method with a single LAC assignment of bone for comparison. The multi-echo images from the acquired mUTE sequence at $TE_3 = 2310 \text{ } \mu\text{s}$ and $TE_4 = 3550 \text{ } \mu\text{s}$ were used as in-phase and out-of-phase images for the two-point Dixon-based method, respectively. The same images were used to generate LAC maps using the atlas-based method¹⁷. The CT image was converted to the LAC at 511 keV using bilinear transformation⁶⁴. Then, PET images were reconstructed with attenuation correction using the LAC maps. All LAC images generated from the MRAC methods were registered to the CT imaging space and then subsequently converted to the PET imaging space prior to reconstruction by using non-rigid registration (with scaling transformation) based on mutual information. The ordered subset expectation maximization (OSEM) algorithm⁶⁵ was used with 3 iterations of 17 subsets to

reconstruct PET images with the following parameters: image size = 128×128×89, in-plane voxel size = 2.34×2.34 mm², and slice-thickness = 2.8 mm.

Analysis

The performance of the proposed mUTE-based MRAC method was evaluated and compared to other MRAC methods, using CT as the ground truth. To evaluate the accuracy of bone LAC estimation, Dice coefficient was calculated for bone using the following equation:

$$Dice\ Coefficient = \frac{2 \cdot |Bone_{MRAC} \cap Bone_{CT}|}{|Bone_{CT}|} \quad [7]$$

where $Bone_{MRAC}$ and $Bone_{CT}$ each denote the bone region defined from the LAC maps from the MRAC methods and CT, respectively. For the in vivo experiment, structural similarity (SSIM) index⁶⁶ was also calculated to assess the similarity of bone LACs between CT and the different MRAC methods that estimate bone LAC. The regions with LAC value above 0.136 cm⁻¹ were identified as bone for this analysis⁶⁷. Joint histograms comparing the PET activity after attenuation correction were generated to evaluate the correlation between the PET images reconstructed from CT and the different MRAC methods. Pearson correlation coefficient (r) was calculated and used to determine the coefficient of determination (r²). SSIM index⁶⁶ was also calculated to assess the similarity between the PET images reconstructed from CT and the different MRAC methods.

For the in vivo experiment, region-of-interest (ROI) analysis was also performed to evaluate the performance of the proposed method across subjects. Regions of four cortex lobes (i.e., frontal, temporal, parietal, occipital), cerebellum, whole white matter (WM) and whole gray matter (GM) determined by the automated anatomical labeling (AAL) template⁶⁸ were evaluated for the analysis. Non-rigid registration (with scaling transformation) based on mutual information was performed to convert the ROIs in the common Montreal Neurological Institute (MNI) space⁶⁹ to the imaging space of each individual subject data. Subsequently, the relative absolute error was calculated for each of the ROI and the different MRAC methods in each individual subject as follows:

$$Relative\ Absolute\ Error = \frac{|PET_{MRAC} - PET_{CT}|}{PET_{CT}} \times 100\% \quad [8]$$

The mean relative absolute error from each ROI was used to calculate the mean and standard deviation across all subjects for the different MRAC methods. Wilcoxon signed rank test was performed to test for significant differences in the performance between the proposed method and the other MRAC methods at significance level of 0.05.

Results

Figure 2, Supplementary Figures S1 and S2 show the results of k-space trajectory correction using the proposed mUTE sequence. Clear differences were observed between the nominal and measured k-space trajectory traversed by the readout gradients in the mUTE sequence (Supplementary Figure S1c). Noticeable differences were also observed between different gradient axes (Supplementary Figure S1c). With k-space trajectory correction, artifacts were noticeably reduced in all of the images produced by the mUTE sequence (Fig. 2 and Supplementary Figure S2).

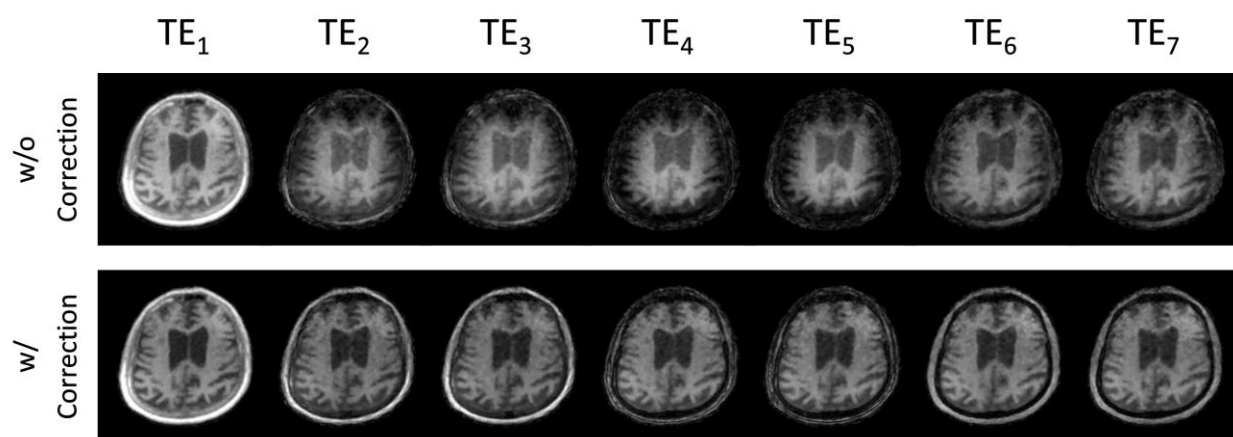


Figure 2. Results of k-space trajectory correction for mUTE sequence. Images of mUTE sequence from the in vivo experiment with and without k-space trajectory correction are shown. Notice the difference in UTE (TE_1) and multi-echo (TE_2, \dots, TE_7) images with and without the k-space trajectory correction.

Figures 3-6 show the results from the phantom experiment. Water, fat, and bone proton density fraction maps were successfully obtained in the expected regions using the proposed mUTE method (Fig. 3). The fraction maps of water and fat obtained from the mUTE method were visually similar to those obtained from the two-point Dixon method, with better separation of water and fat in the gelatin region (Fig. 3). Visually, the LAC map generated from the mUTE method was similar to those from CT, capturing the continuous variation well especially within the bone regions (Fig. 4). The Dice coefficient of bone from the mUTE method was 0.76. The PET images reconstructed from the mUTE method were also similar to those from CT (Fig. 5a), showing lower error compared to those from the two-point Dixon-based method (Fig. 5b). Similar findings were observed in the joint histogram results, with the PET activity reconstructed from the mUTE method showing the best correlation in relation to those reconstructed from CT (Fig. 6). The coefficients of determination (r^2) between the reconstructed PET images from CT and the different MRAC methods were 0.97 and 0.99 for Dixon-based method and mUTE method, respectively. The SSIM index between the reconstructed PET images from CT and the different MRAC methods were 0.92 and 0.98 for Dixon-based method and mUTE method, respectively.

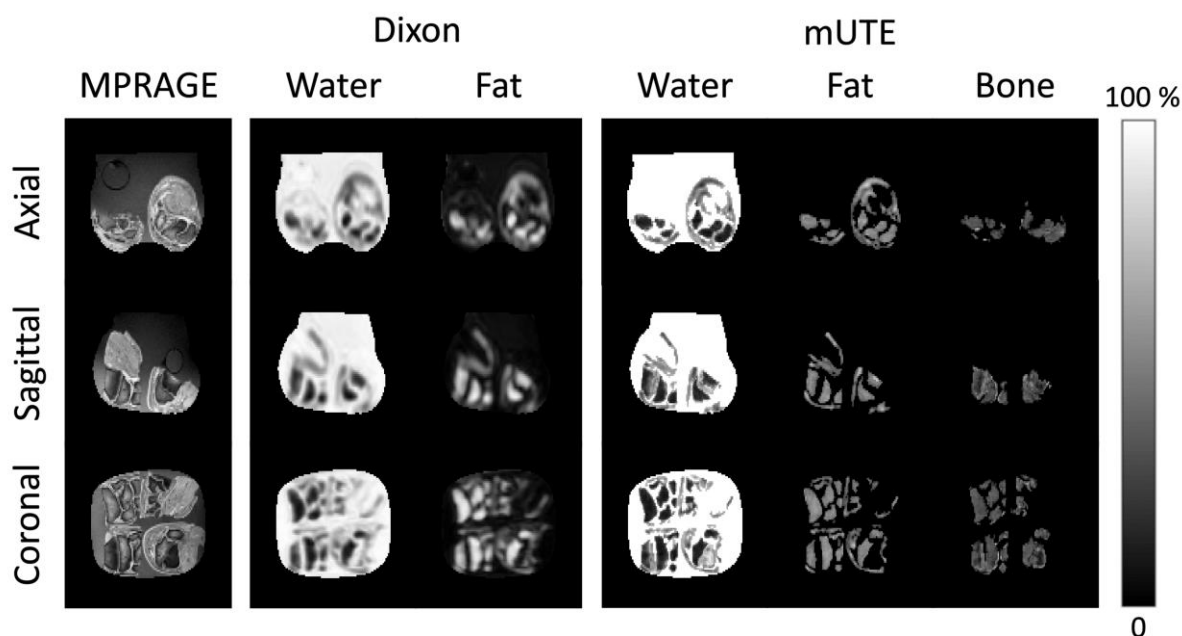


Figure 3. Results of quantification from the phantom experiment. MPRAGE images, water and fat proton density fraction maps from the two-point Dixon method, and water, fat, and bone proton density fraction maps from the proposed mUTE method are shown.

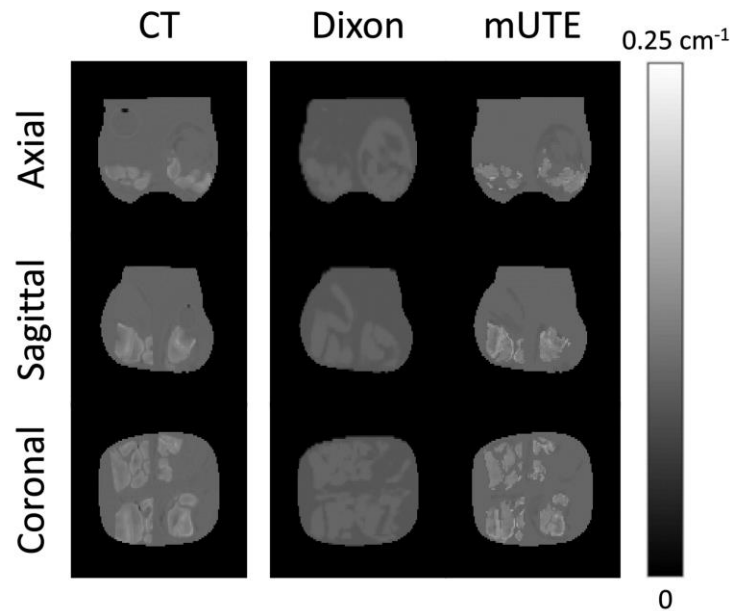


Figure 4. Results of LAC maps from the phantom experiment. LAC maps derived from CT, two-point Dixon-based method, and the proposed mUTE method are shown.

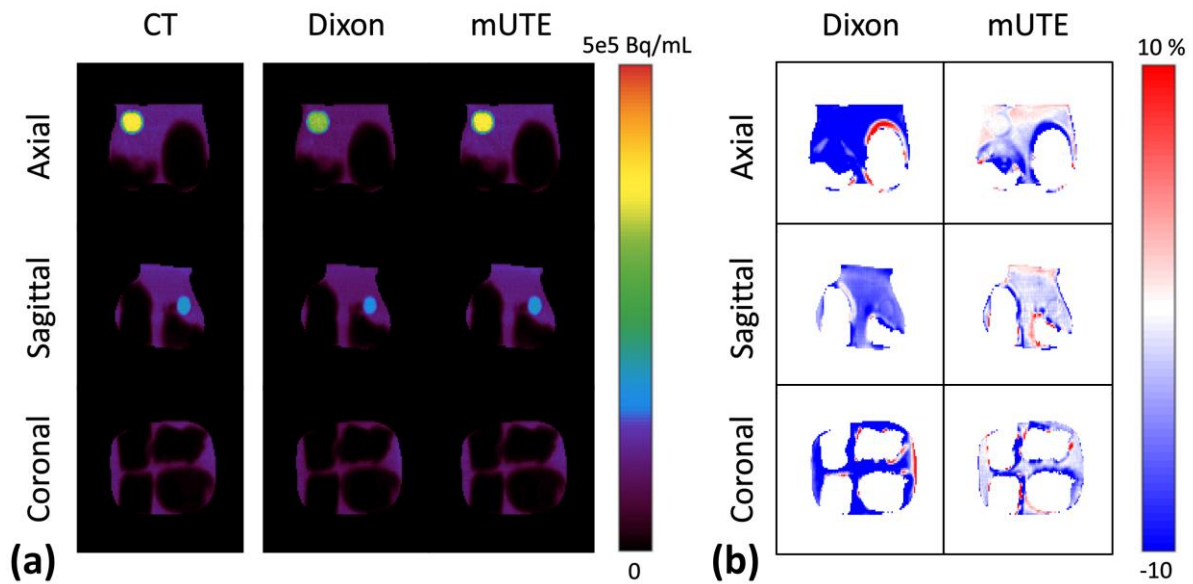


Figure 5. Results of PET reconstruction and percentage error maps from the phantom experiment. **a:** PET images reconstructed using LAC maps derived from CT, two-point Dixon-based method, and the proposed mUTE method. **b:** PET percentage error maps for two-point Dixon-based and the proposed mUTE method.

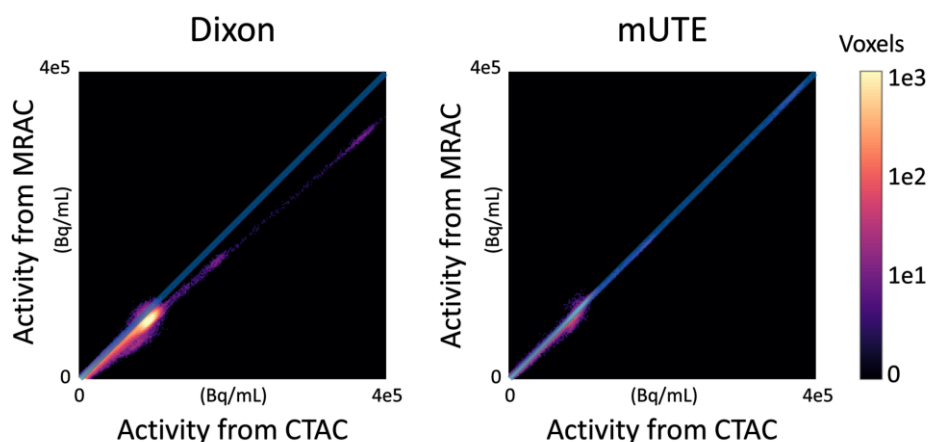


Figure 6. Joint histogram analysis results from the phantom experiment. Logarithmic plots of the joint histogram comparing PET activity after attenuation correction between CT and two-point Dixon-based method, and CT and proposed mUTE method are shown. The reference solid line (blue) represents perfect correlation.

In vivo experiment results from a representative subject (Subject #1) are shown in Figures 7-11 and group analysis are shown in Figure 12 and Table 1. Similar to the phantom study results, water, fat, and bone proton density fraction maps were successfully obtained in the expected regions using the proposed mUTE method (Fig. 7 and Supplementary Figure S3). The fraction maps of water and fat obtained from the mUTE method were visually similar to those obtained from the two-point Dixon method, with better separation of water and fat in the brain tissue region (Fig. 7). The LAC map generated from the mUTE method with continuous LAC assignment of bone was visually most similar to those from CT, with better identification of bone/air regions and continuous variation in LAC compared to that from the atlas-based method (Fig. 8). Table 1 summarizes the Dice coefficient and SSIM index of bone LAC for each subjects along with the group results. As can be seen, the mUTE method with continuous LAC assignment of bone achieves higher Dice coefficient and SSIM index than all the other compared methods.

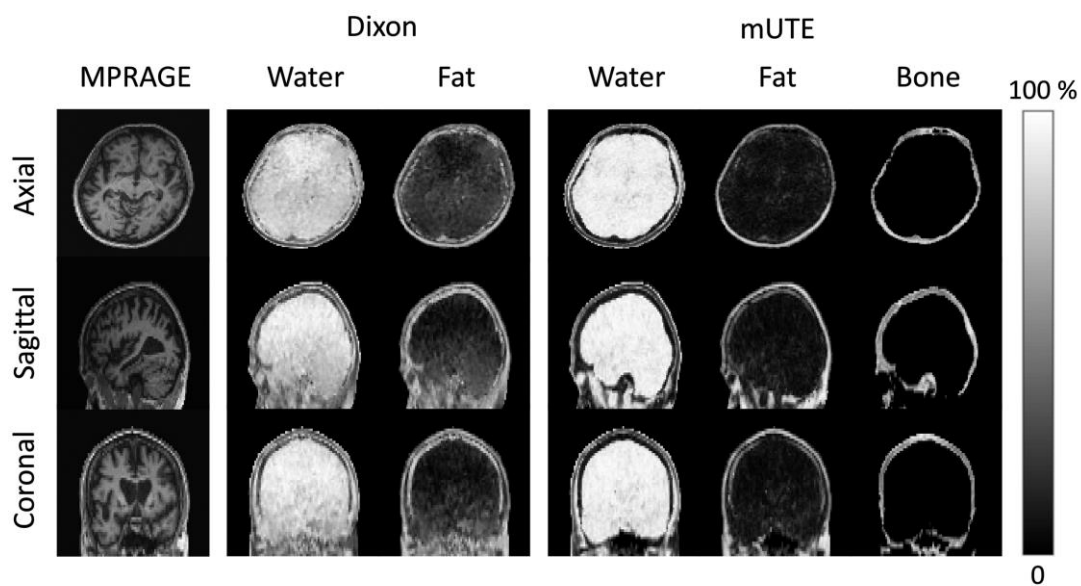


Figure 7. Results of quantification from the in vivo experiment (Subject #1). MPRAGE images, water and fat proton density fraction maps from the two-point Dixon method, and water, fat, and bone proton density fraction maps from the proposed mUTE method are shown.

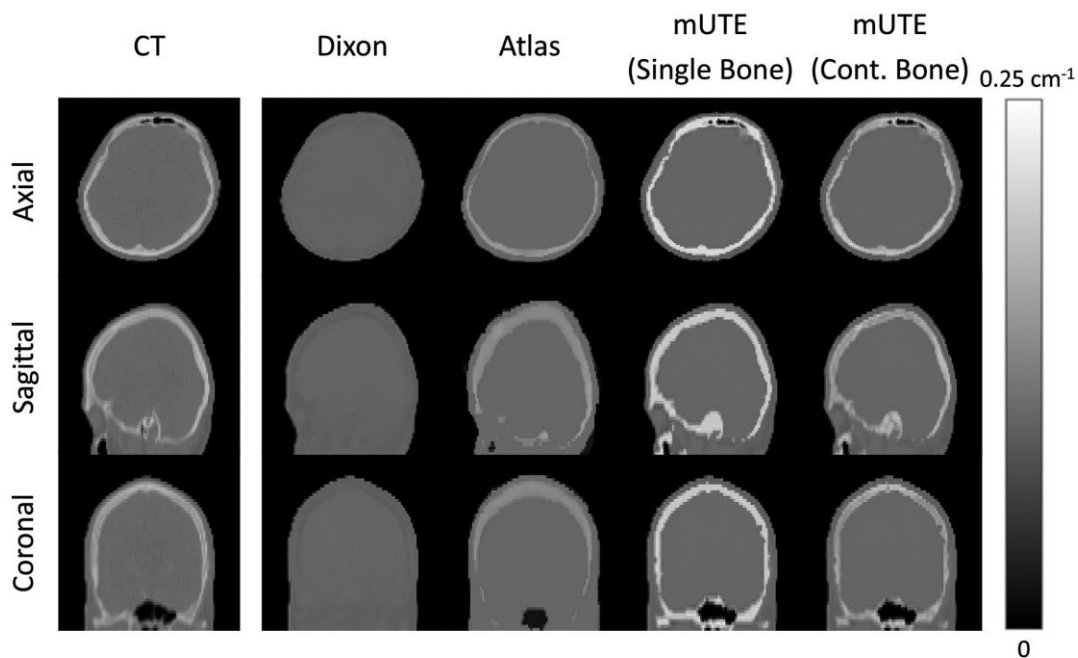


Figure 8. Results of LAC maps from the in vivo experiment (Subject #1). LAC maps derived from CT, two-point Dixon-based method, atlas-based method, proposed mUTE method with single LAC assignment of bone, and proposed mUTE method with continuous LAC assignment of bone are shown.

Table 1. Quantitative Analysis of AC Map from In Vivo Experiment

	Dice Coefficient of Bone			Structural Similarity (SSIM) Index of Bone		
	Atlas	mUTE	mUTE	Atlas	mUTE	mUTE
		(Single Bone)	(Cont. Bone)		(Single Bone)	(Cont. Bone)
Subject #1	0.56	0.75	0.77	0.74	0.70	0.82
Subject #2	0.56	0.76	0.78	0.66	0.65	0.80
Subject #3	0.42	0.66	0.69	0.66	0.64	0.78
Subject #4	0.59	0.88	0.90	0.77	0.77	0.90
Subject #5	0.47	0.76	0.77	0.69	0.67	0.82
Subject #6	0.36	0.88	0.90	0.72	0.80	0.88
Group	0.50 ± 0.09	0.78 ± 0.08	0.80 ± 0.07	0.71 ± 0.04	0.70 ± 0.06	0.83 ± 0.04

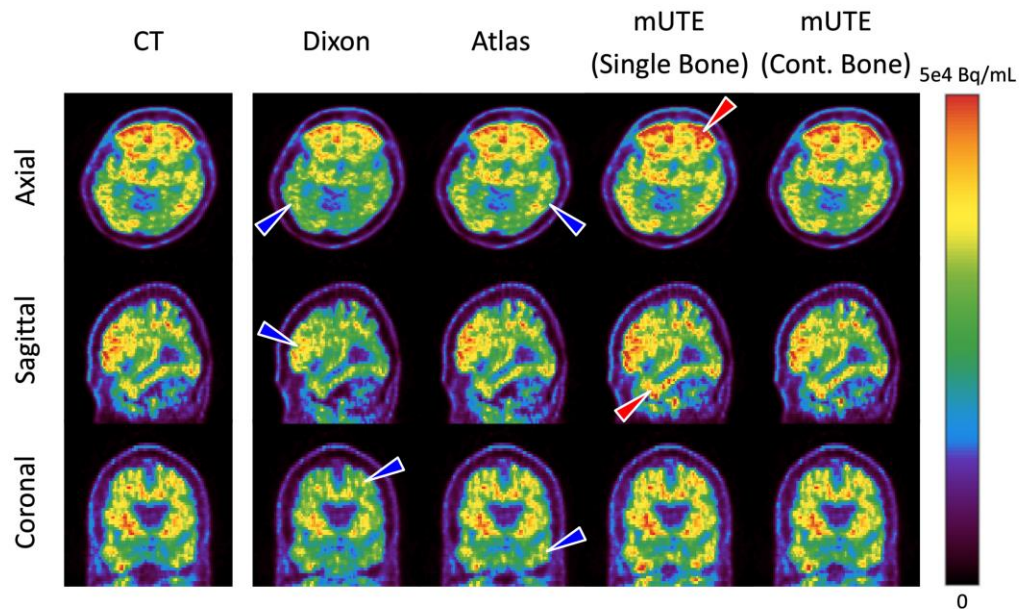


Figure 9. Results of PET reconstruction from the in vivo experiment (Subject #1). PET images reconstructed using LAC maps derived from CT, two-point Dixon-based method, atlas-based method, proposed mUTE method with single LAC assignment of bone, and proposed mUTE method with continuous LAC assignment of bone are shown. Notice regions of underestimated PET activity using Dixon- and atlas-based methods (blue arrowhead) and overestimated PET activity using mUTE method with single LAC assignment of bone (red arrowhead).

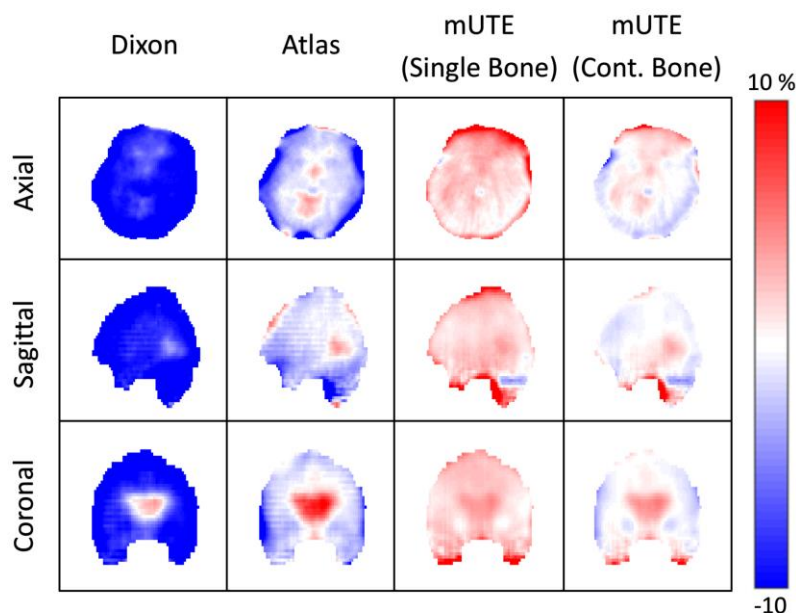


Figure 10. Results of PET percentage error maps from the in vivo experiment (Subject #1). PET percentage error maps from two-point Dixon-based method, atlas-based method, proposed mUTE method with single LAC assignment for bone, and proposed mUTE method with continuous LAC assignment for bone are shown.

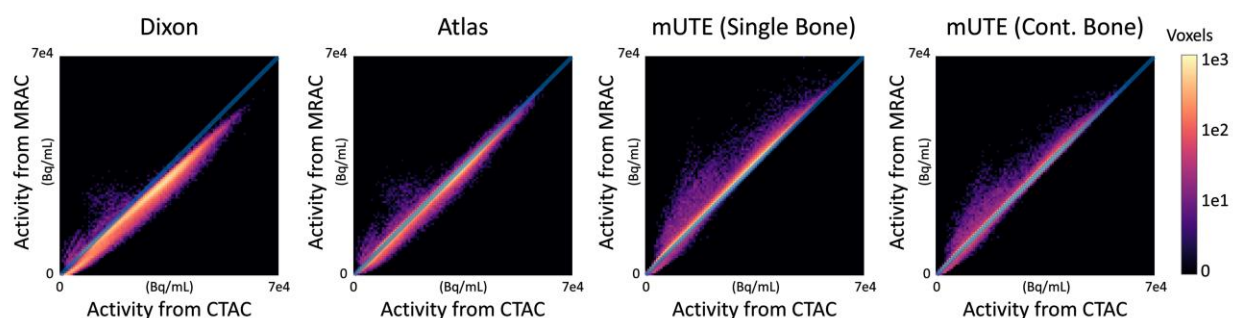


Figure 11. Joint histogram analysis results from the in vivo experiment (Subject #1). Logarithmic plots of the joint histogram comparing PET activity after attenuation correction between CT and the two-point Dixon-based method, CT and the atlas-based method, CT and the proposed mUTE method with single LAC assignment of bone, and CT and the proposed mUTE method with continuous LAC assignment of bone. The reference solid line (blue) represents perfect correlation.

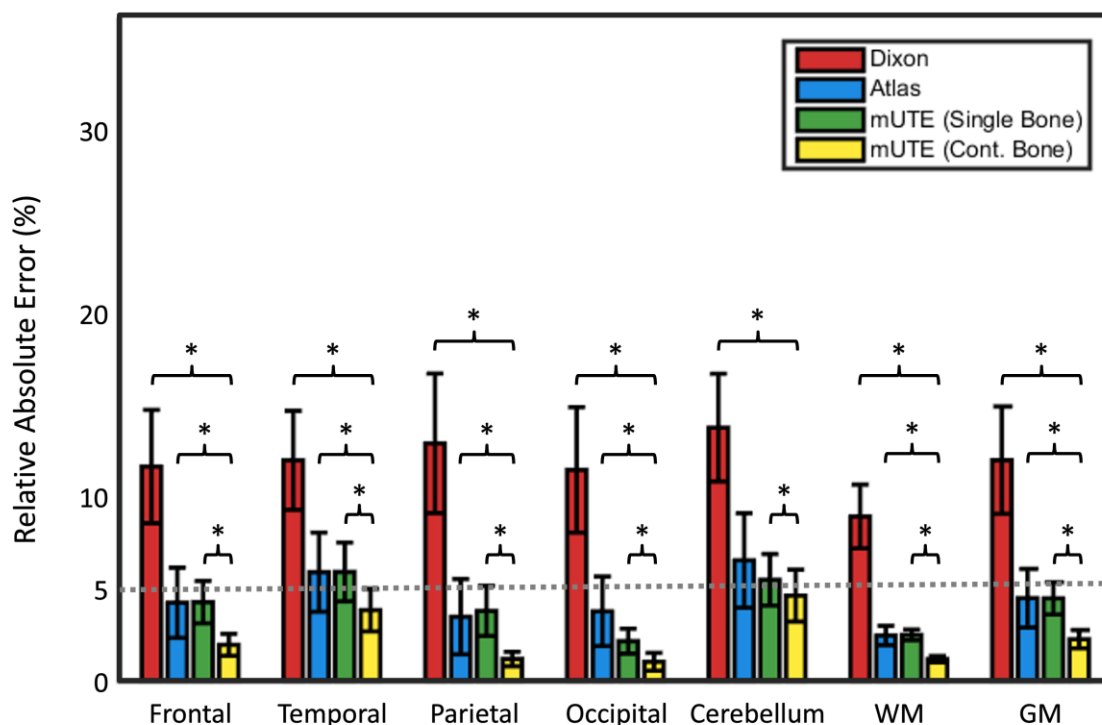


Figure 12. ROI analysis result of relative absolute error across all subjects. Relative absolute error calculated at different ROIs across all subjects ($n=6$) for the two-point Dixon-based method (red), atlas-based method (blue), proposed mUTE method with single LAC assignment of bone (green), and proposed mUTE method with continuous LAC assignment of bone (yellow) are shown along with a reference line at relative error of 5% (gray dashed line). Note that results from using CT for attenuation correction were used as the ground truth for the calculation of relative absolute error. The asterisks denote a statistically significant difference between the proposed method and the other MRAC method at significance level of 0.05.

The PET images reconstructed from the mUTE method with continuous LAC assignment of bone were also similar to those from CT (Fig. 9), showing an overall lowest error across regions compared to those from other MRAC methods (Fig. 10). The PET images reconstructed from the Dixon-based and atlas-based methods showed relatively high underestimation of PET activity in the cortex regions (blue arrowheads in Fig. 9), whereas those from the mUTE method with single LAC assignment of bone showed relatively high overestimation of PET activity in the cortex

regions (red arrowheads in Fig. 9). Supplementary Table 1 summarizes the regional mean relative absolute error of the reconstructed PET images from Subject #1 along with the group results. Similar trends were observed in the joint histogram results, with the PET activity reconstructed from the mUTE method showing higher correlation with those reconstructed from CT compared to other methods (Fig. 11). The coefficient of determination (r^2) between the reconstructed PET images from CT and the different MRAC methods were 0.95 ± 0.02 , 0.96 ± 0.02 , 0.95 ± 0.01 , and 0.97 ± 0.01 for Dixon-based method, atlas-based method, mUTE method with single LAC assignment of bone, and mUTE method with continuous LAC assignment of bone, respectively. The SSIM index between the reconstructed PET images from CT and the different MRAC methods were 0.95 ± 0.02 , 0.98 ± 0.01 , 0.98 ± 0.01 , and 0.99 ± 0.01 for the Dixon-based method, atlas-based method, mUTE method with single LAC assignment of bone, and mUTE method with continuous LAC assignment of bone, respectively. The ROI analysis (Fig. 12) showed the best performance for the mUTE method with continuous LAC assignment of bone, resulting in mean relative absolute error below 5% with the lowest standard deviation compared to other methods in all of the ROIs. Statistically significant differences were observed between the proposed method and the other MRAC methods at all ROIs, except the cerebellum which did not show a statistically significant difference between the proposed method and the atlas-based method.

Discussion

In this work, a physical model-based MRAC method is proposed for PET/MR. UTE and multi-echo Dixon images are used with a physical compartmental model to estimate the fractions of water, fat and bone components, which are subsequently used to estimate the continuous LAC maps for PET attenuation correction. Although the combination of UTE/ZTE with Dixon has been proposed in the past for PET attenuation correction^{13,14,33,70}, the current work differs from previous approaches in the sense that (i) a new sequence integrating 3D UTE with multi-echo Dixon imaging in a single acquisition is developed, (ii) a general physical compartmental model is used to estimate the signal from the different compartments of water, fat and bone altogether, and (iii) continuous variation of LAC is estimated via the different proportions of compartments. The proposed method does not require prior anatomical structure information for LAC estimation and is robust to B_0 and receive B_1 effects.

The proposed method showed better performance in comparison to the conventional Dixon-based and atlas-based MRAC methods, in both the phantom and in vivo human studies. The proposed method not only reconstructed PET images with higher correlation and similarity, but also with lower mean and standard deviation of relative absolute error across different ROIs and subjects compared to other MRAC methods (Fig. 12). Since the choice of LACs for different compartments may influence the magnitude of relative absolute error but not the variation, assessing the variation of error may be more important in evaluating the accuracy of PET attenuation correction methods. Although tested from a small number of subjects ($n=6$), the current study showed the smallest variation of relative absolute error using the proposed method (Fig. 12), indicating better PET attenuation correction. However, the proposed method did not show statistically significant difference compared to the atlas-based MRAC method for the cerebellum, which is presumed to be due to the small number of subjects ($n=6$). Further investigations are necessary in increased number of subjects to confirm the findings from this work regarding the performance of the proposed method.

Trajectory correction is necessary to accurately reconstruct the UTE and multi-echo Dixon images and estimate the different compartments using the proposed method. Since the k-space trajectory traversed by the readout gradients of mUTE can be different for each gradient axis due to the distortion by hardware imperfections and eddy current effects (Supplementary Figure S1c), a simple gradient delay correction⁷¹ may not be sufficient for accurate image reconstruction (Supplementary Figure S2). The k-space trajectory can be measured from all three gradient axes to improve the performance of correction (Supplementary Figure S2). Note that, the employed trajectory correction method is intrinsically robust to phase-wrapping by design: phase wrap-around effects can be minimized by determining $\emptyset(t)$ recursively from $\emptyset(\Delta t_N)$, since $\emptyset_G(\Delta t_N) = \emptyset_G(t_N) - \emptyset_G(t_{N-1})$ will always be lower than π as long as the sampling frequency satisfies the Nyquist limit for the gradient structure of interest. It must be noted that the number of phase-encodings (N_{PE}) in the employed trajectory correction sequence must be chosen carefully to satisfy $N_{PE} \geq \max\{k_G(t)\} \cdot \text{FOV}$, to properly resolve a phase shift of π produced over each voxel at the maximum value of $k_G(t)$ ⁷².

The current work has several limitations. The effects of T_1 and flip angle were neglected in the proposed signal model for parameter estimation, which may not be negligible when the flip

angle is not small enough or TR is not short enough as in the current study. However, this error may not be a problem for PET attenuation correction, since the ratio between the estimated parameters is evaluated for the generation of LAC maps. This error can be mitigated by choosing a smaller flip angle and shorter TR for acquisition, or by acquiring a separate acquisition with T_1 mapping. Another source of error exists in the estimation of the short- T_2 component. In the current work, the R_2^* effect due to short- T_2 component was neglected and the proton density of bone was estimated relying on a single UTE acquisition. This issue can be potentially resolved by modifying the sequence to acquire a larger number of UTE images at different TE times and taking into account the R_2^* effect due to the short- T_2 component. Also, in the current work the MR scans for the in vivo experiments were conducted using an MR scanner instead of a PET/MR scanner, due to the clinical workflow and associated study protocol. However, we don't expect any major difference between the mUTE images obtained from the MR scanner and the PET/MR scanner, since the mUTE sequence used in the in vivo experiments on the MR scanner was implemented with the same hardware constraints (i.e., minimum TE, maximum gradient strengths and maximum gradient slew rates) as the mUTE sequence used in the phantom experiment on the PET/MR scanner. We have also carried out phantom experiments to compare the signal-to-noise ratio (SNR) of the images acquired on the two scanners using the same phantom and same sequence and found very comparable SNRs (results not shown). Nevertheless, further investigation with in vivo experiments may be necessary to further validate the performance of the proposed method on PET/MR scanners. Lastly, in the current work CT-based attenuation correction map was used as the ground truth reference for comparison, which may contain systematic bias that can result in overestimation of the PET activity⁷³. Further comparisons with attenuation maps from 511 keV transmission scans may be necessary to accurately characterize the performance of the proposed method.

Several aspects of the proposed method can be further improved. In this work, the TE times and the number of echoes were chosen arbitrarily for UTE and the multi-echo Dixon images (i.e., one UTE and six multi-echo Dixon acquisitions for robust fat-water separation). Cramér–Rao bound (CRB) analysis can be performed to determine the optimal TE times/number of echoes and improve the estimation performance of the proposed method. The acquisition time of the proposed method may also be further reduced through optimizations. For example, for the case of the proposed physical model where five parameters need to be estimated, signal from five echoes

(including UTE) are needed at minimum which can reduce the scan time further (e.g., scan time reduction by 25%). A preliminary study was performed to demonstrate the feasibility of the proposed method using only five echoes (Supplementary Figure S4), which requires further investigation for validation. More advanced image reconstruction with higher under-sampling factor can reduce the scan time further. Also, a voxel-based least squares approach is used in the current work to estimate the parameters. Parameter estimation can be further improved with enhanced robustness to B_0 inhomogeneity using joint estimation with constraints⁷⁴, with and without region-growing⁷⁵ or graph-cut algorithms⁷⁶. Moreover, the proposed approach is not mutually exclusive to other methods and can potentially be improved by combining with other approaches. In this work, segmentation was used as a preprocessing step to improve the delineation of bone and air, i.e., by using bone-enhanced image for bone¹⁰ and applying a differential thresholding strategy to the frontal sinus region for air³⁴. Similarly, the proposed approach can be further improved by additionally utilizing information from bone-enhanced images generated from different strategies^{11,13}, and by incorporating a more rigorous region-based differential thresholding strategy for the delineation of air, especially for regions such as the ethmoidal sinuses, nasal septa and mastoid process³⁷. Also, combination with DNN-based algorithms may further improve the performance of the proposed method. Recently, DNN-based algorithms utilizing information from both ZTE and two-point Dixon have been developed and showed outstanding performance for MR-based PET attenuation correction in the brain⁴⁷ and pelvis^{44,45} regions. Since the proposed method allows acquisition of multiple images of UTE and multi-echo Dixon along with additional information such as the proton densities of different compartments as well as B_0 and R_2^* via parameter estimation (Supplementary Figure S3), the proposed method has great potential to work well with DNN-based algorithms.

The proposed method may be extended for application to other parts of the body. However, several technical challenges may arise. First, the greater variety of tissue types need to be considered. For instance, trabecular bone in the body consists of more water and fat components compared to cortical bone (e.g., bone in the skull) due to the porous structure filled with bone marrow and blood vessels. More complicated compartmental model may be needed for the proposed method to handle trabecular bone and/or the different tissue types. Second, respiratory motion may be a concern. This issue could be addressed by further accelerating the imaging speed and by the usage of breath-hold. Third, B_0 inhomogeneity in other body parts may be more severe

than the brain and could be a concern. The proposed method uses multi-echo Dixon method for water/fat separation and is relatively robust to B_0 inhomogeneity. Further investigation is necessary to verify the feasibility of the proposed method to other body regions.

Conclusions

A physical compartmental model-based MRAC method was developed for PET/MR. The proposed method generates subject-specific, continuous LAC maps for quantitative PET image reconstruction in PET/MR.

Acknowledgements

This work was supported in part by the National Institutes of Health (T32EB013180, R01CA165221, R01HL118261, R21EB021710, and P41EB022544) and the Federal Share of Program Income earned by the Massachusetts General Hospital on C06CA059267.

Conflict of Interest

The authors have no relevant conflicts of interest to disclose.

References

1. Catana C, Benner T, van der Kouwe A, et al. MRI-assisted PET motion correction for neurologic studies in an integrated MR-PET scanner. *J Nucl Med*. 2011;52(1):154-161.
2. Petibon Y, Ouyang J, Zhu X, et al. Cardiac motion compensation and resolution modeling in simultaneous PET-MR: a cardiac lesion detection study. *Phys Med Biol*. 2013;58(7):2085-2102.
3. Petibon Y, Guehl NJ, Reese TG, et al. Impact of motion and partial volume effects correction on PET myocardial perfusion imaging using simultaneous PET-MR. *Phys Med Biol*. 2017;62(2):326-343.
4. Catana C, Guimaraes AR, Rosen BR. PET and MR imaging: the odd couple or a match made in heaven? *J Nucl Med*. 2013;54(5):815-824.

5. Mehranian A, Arabi H, Zaidi H. Vision 20/20: magnetic resonance imaging-guided attenuation correction in PET/MRI: challenges, solutions, and opportunities. *Med Phys*. 2016;43(3):1130-1155.
6. Izquierdo-Garcia D, Catana C. MR Imaging-Guided Attenuation Correction of PET Data in PET/MR Imaging. *PET Clin*. 2016;11(2):129-149.
7. Schulz V, Torres-Espallardo I, Renisch S, et al. Automatic, three-segment, MR-based attenuation correction for whole-body PET/MR data. *Eur J Nucl Med Mol Imaging*. 2011;38(1):138-152.
8. Martinez-Moller A, Souvatzoglou M, Delso G, et al. Tissue classification as a potential approach for attenuation correction in whole-body PET/MRI: evaluation with PET/CT data. *J Nucl Med*. 2009;50(4):520-526.
9. Wollenweber SD, Ambwani S, Lonn AHR, et al. Comparison of 4-class and continuous fat/water methods for whole-body, MR-based PET attenuation correction. *IEEE Transactions on Nuclear Science*. 2013;60(5):3391-3398.
10. Catana C, van der Kouwe A, Benner T, et al. Toward implementing an MRI-based PET attenuation-correction method for neurologic studies on the MR-PET brain prototype. *J Nucl Med*. 2010;51(9):1431-1438.
11. Keereman V, Fierens Y, Broux T, De Deene Y, Lonneux M, Vandenberghe S. MRI-based attenuation correction for PET/MRI using ultrashort echo time sequences. *J Nucl Med*. 2010;51(5):812-818.
12. An HJ, Seo S, Kang H, et al. MRI-Based Attenuation Correction for PET/MRI Using Multiphase Level-Set Method. *J Nucl Med*. 2016;57(4):587-593.
13. Berker Y, Franke J, Salomon A, et al. MRI-based attenuation correction for hybrid PET/MRI systems: a 4-class tissue segmentation technique using a combined ultrashort-echo-time/Dixon MRI sequence. *J Nucl Med*. 2012;53(5):796-804.
14. Jang H, Liu F, Bradshaw T, McMillan AB. Rapid dual-echo ramped hybrid encoding MR-based attenuation correction (dRHE-MRAC) for PET/MR. *Magn Reson Med*. 2018;79(6):2912-2922.
15. Ouyang J, Chun SY, Petibon Y, Bonab AA, Alpert N, Fakhri GE. Bias atlases for segmentation-based PET attenuation correction using PET-CT and MR. *IEEE Trans Nucl Sci*. 2013;60(5):3373-3382.
16. Hofmann M, Steinke F, Scheel V, et al. MRI-based attenuation correction for PET/MRI: a novel approach combining pattern recognition and atlas registration. *J Nucl Med*. 2008;49(11):1875-1883.

17. Wollenweber SD, Ambwani S, Delso G, et al. Evaluation of an atlas-based PET head attenuation correction using PET/CT & MR patient data. *IEEE Transactions on Nuclear Science*. 2013;60(5):3383-3390.
18. Burgos N, Cardoso MJ, Thielemans K, et al. Attenuation correction synthesis for hybrid PET-MR scanners: application to brain studies. *IEEE Trans Med Imaging*. 2014;33(12):2332-2341.
19. Arabi H, Zaidi H. Magnetic resonance imaging-guided attenuation correction in whole-body PET/MRI using a sorted atlas approach. *Med Image Anal*. 2016;31:1-15.
20. Johansson A, Karlsson M, Nyholm T. CT substitute derived from MRI sequences with ultrashort echo time. *Med Phys*. 2011;38(5):2708-2714.
21. Navalpakkam BK, Braun H, Kuwert T, Quick HH. Magnetic resonance-based attenuation correction for PET/MR hybrid imaging using continuous valued attenuation maps. *Invest Radiol*. 2013;48(5):323-332.
22. Huynh T, Gao Y, Kang J, et al. Estimating CT Image From MRI Data Using Structured Random Forest and Auto-Context Model. *IEEE Trans Med Imaging*. 2016;35(1):174-183.
23. Roy S, Wang WT, Carass A, Prince JL, Butman JA, Pham DL. PET attenuation correction using synthetic CT from ultrashort echo-time MR imaging. *J Nucl Med*. 2014;55(12):2071-2077.
24. Andreasen D, Van Leemput K, Hansen RH, Andersen JA, Edmund JM. Patch-based generation of a pseudo CT from conventional MRI sequences for MRI-only radiotherapy of the brain. *Med Phys*. 2015;42(4):1596-1605.
25. Chen Y, Juttukonda M, Su Y, et al. Probabilistic Air Segmentation and Sparse Regression Estimated Pseudo CT for PET/MR Attenuation Correction. *Radiology*. 2015;275(2):562-569.
26. Torrado-Carvajal A, Herraiz JL, Alcain E, et al. Fast Patch-Based Pseudo-CT Synthesis from T1-Weighted MR Images for PET/MR Attenuation Correction in Brain Studies. *J Nucl Med*. 2016;57(1):136-143.
27. Anazodo UC, Thiessen JD, Ssali T, et al. Feasibility of simultaneous whole-brain imaging on an integrated PET-MRI system using an enhanced 2-point Dixon attenuation correction method. *Front Neurosci*. 2014;8:434.
28. Poynton CB, Chen KT, Chonde DB, et al. Probabilistic atlas-based segmentation of combined T1-weighted and DUTE MRI for calculation of head attenuation maps in integrated PET/MRI scanners. *Am J Nucl Med Mol Imaging*. 2014;4(2):160-171.

29. Izquierdo-Garcia D, Hansen AE, Forster S, et al. An SPM8-based approach for attenuation correction combining segmentation and nonrigid template formation: application to simultaneous PET/MR brain imaging. *J Nucl Med*. 2014;55(11):1825-1830.
30. Baran J, Chen Z, Sforazzini F, et al. Accurate hybrid template-based and MR-based attenuation correction using UTE images for simultaneous PET/MR brain imaging applications. *BMC Med Imaging*. 2018;18(1):41.
31. Delso G, Kemp B, Kaushik S, Wiesinger F, Sekine T. Improving PET/MR brain quantitation with template-enhanced ZTE. *NeuroImage*. 2018;181:403-413.
32. Khalife M, Fernandez B, Jaubert O, et al. Subject-specific bone attenuation correction for brain PET/MR: can ZTE-MRI substitute CT scan accurately? *Phys Med Biol*. 2017;62(19):7814-7832.
33. Leynes AP, Yang J, Shanbhag DD, et al. Hybrid ZTE/Dixon MR-based attenuation correction for quantitative uptake estimation of pelvic lesions in PET/MRI. *Med Phys*. 2017;44(3):902-913.
34. Yang J, Wiesinger F, Kaushik S, et al. Evaluation of Sinus/Edge-Corrected Zero-Echo-Time-Based Attenuation Correction in Brain PET/MRI. *J Nucl Med*. 2017;58(11):1873-1879.
35. Wiesinger F, Bylund M, Yang J, et al. Zero TE-based pseudo-CT image conversion in the head and its application in PET/MR attenuation correction and MR-guided radiation therapy planning. *Magn Reson Med*. 2018;80(4):1440-1451.
36. Juttukonda MR, Mersereau BG, Chen Y, et al. MR-based attenuation correction for PET/MRI neurological studies with continuous-valued attenuation coefficients for bone through a conversion from R2* to CT-Hounsfield units. *NeuroImage*. 2015;112:160-168.
37. Ladefoged CN, Benoit D, Law I, et al. Region specific optimization of continuous linear attenuation coefficients based on UTE (RESOLUTE): application to PET/MR brain imaging. *Phys Med Biol*. 2015;60(20):8047-8065.
38. Cabello J, Lukas M, Forster S, Pyka T, Nekolla SG, Ziegler SI. MR-based attenuation correction using ultrashort-echo-time pulse sequences in dementia patients. *J Nucl Med*. 2015;56(3):423-429.
39. Santos Ribeiro A, Rota Kops E, Herzog H, Almeida P. Hybrid approach for attenuation correction in PET/MR scanners. *Nuclear Instruments and Methods in Physics Research A*. 2014;734:166-170.
40. Nie D, Trullo R, Lian J, et al. Medical Image Synthesis with Context-Aware Generative Adversarial Networks. *Med Image Comput Comput Assist Interv*. 2017;10435:417-425.
41. Arabi H, Zeng G, Zheng G, Zaidi H. Novel adversarial semantic structure deep learning for MRI-guided attenuation correction in brain PET/MRI. *Eur J Nucl Med Mol Imaging*. 2019;46(13):2746-2759.

42. Liu F, Jang H, Kijowski R, Bradshaw T, McMillan AB. Deep Learning MR Imaging-based Attenuation Correction for PET/MR Imaging. *Radiology*. 2018;286(2):676-684.
43. Han X. MR-based synthetic CT generation using a deep convolutional neural network method. *Med Phys*. 2017;44(4):1408-1419.
44. Leynes AP, Yang J, Wiesinger F, et al. Zero-Echo-Time and Dixon Deep Pseudo-CT (ZeDD CT): Direct Generation of Pseudo-CT Images for Pelvic PET/MRI Attenuation Correction Using Deep Convolutional Neural Networks with Multiparametric MRI. *J Nucl Med*. 2018;59(5):852-858.
45. Torrado-Carvajal A, Vera-Olmos J, Izquierdo-Garcia D, et al. Dixon-VIBE Deep Learning (DIVIDE) Pseudo-CT Synthesis for Pelvis PET/MR Attenuation Correction. *J Nucl Med*. 2019;60(3):429-435.
46. Spuhler KD, Gardus J, 3rd, Gao Y, DeLorenzo C, Parsey R, Huang C. Synthesis of Patient-Specific Transmission Data for PET Attenuation Correction for PET/MRI Neuroimaging Using a Convolutional Neural Network. *J Nucl Med*. 2019;60(4):555-560.
47. Gong K, Yang J, Kim K, El Fakhri G, Seo Y, Li Q. Attenuation correction for brain PET imaging using deep neural network based on Dixon and ZTE MR images. *Phys Med Biol*. 2018;63(12):125011.
48. Glover GH, Pauly JM, Bradshaw KM. Boron-11 imaging with a three-dimensional reconstruction method. *J Magn Reson Imaging*. 1992;2(1):47-52.
49. Dixon WT. Simple proton spectroscopic imaging. *Radiology*. 1984;153(1):189-194.
50. Glover GH. Multipoint Dixon technique for water and fat proton and susceptibility imaging. *J Magn Reson Imaging*. 1991;1(5):521-530.
51. Hamilton G, Yokoo T, Bydder M, et al. In vivo characterization of the liver fat (1)H MR spectrum. *NMR Biomed*. 2011;24(7):784-790.
52. Hamilton G, Schlein AN, Middleton MS, et al. In vivo triglyceride composition of abdominal adipose tissue measured by (1) H MRS at 3T. *J Magn Reson Imaging*. 2017;45(5):1455-1463.
53. Yu H, Shimakawa A, McKenzie CA, Brodsky E, Brittain JH, Reeder SB. Multiecho water-fat separation and simultaneous R2* estimation with multifrequency fat spectrum modeling. *Magn Reson Med*. 2008;60(5):1122-1134.
54. Yu H, Shimakawa A, Hines CD, et al. Combination of complex-based and magnitude-based multiecho water-fat separation for accurate quantification of fat-fraction. *Magn Reson Med*. 2011;66(1):199-206.
55. Fessler JA, Sutton BP. Nonuniform fast Fourier transforms using min-max interpolation. 2003.
56. Pruessmann KP, Weiger M, Scheidegger MB, Boesiger P. SENSE: sensitivity encoding for fast MRI. *Magn Reson Med*. 1999;42(5):952-962.

57. Pruessmann KP, Weiger M, Bornert P, Boesiger P. Advances in sensitivity encoding with arbitrary k-space trajectories. *Magn Reson Med*. 2001;46(4):638-651.
58. Chambolle A. An algorithm for total variation minimization and applications. *Journal of Mathematical imaging and vision*. 2004;20(1-2):89-97.
59. Vogel CR. *Computational methods for inverse problems*. Vol 23: Siam; 2002.
60. Golub G, Pereyra V. Separable nonlinear least squares: the variable projection method and its applications. *Inverse problems*. 2003;19(2):R1.
61. Wiesinger F, Sacolick LI, Menini A, et al. Zero TE MR bone imaging in the head. *Magn Reson Med*. 2016;75(1):107-114.
62. Schneider W, Bortfeld T, Schlegel W. Correlation between CT numbers and tissue parameters needed for Monte Carlo simulations of clinical dose distributions. *Phys Med Biol*. 2000;45(2):459-478.
63. Tofts PS. PD: proton density of tissue water. *Quantitative MRI of the brain: measuring changes caused by disease*. 2003.85-109.
64. Carney JP, Townsend DW, Rappoport V, Bendriem B. Method for transforming CT images for attenuation correction in PET/CT imaging. *Med Phys*. 2006;33(4):976-983.
65. Hudson HM, Larkin RS. Accelerated image reconstruction using ordered subsets of projection data. *IEEE Trans Med Imaging*. 1994;13(4):601-609.
66. Wang Z, Bovik AC, Sheikh HR, Simoncelli EP. Image quality assessment: from error visibility to structural similarity. *IEEE Trans Image Process*. 2004;13(4):600-612.
67. Zaidi H, Montandon ML, Slosman DO. Magnetic resonance imaging-guided attenuation and scatter corrections in three-dimensional brain positron emission tomography. *Med Phys*. 2003;30(5):937-948.
68. Tzourio-Mazoyer N, Landeau B, Papathanassiou D, et al. Automated anatomical labeling of activations in SPM using a macroscopic anatomical parcellation of the MNI MRI single-subject brain. *NeuroImage*. 2002;15(1):273-289.
69. Fonov VS, Evans AC, McKinsty RC, Almlí C, Collins D. Unbiased nonlinear average age-appropriate brain templates from birth to adulthood. *NeuroImage*. 2009. (47):S102.
70. Su KH, Hu L, Stehning C, et al. Generation of brain pseudo-CTs using an undersampled, single-acquisition UTE-mDixon pulse sequence and unsupervised clustering. *Med Phys*. 2015;42(8):4974-4986.

71. Speier P, Trautwein F. Robust radial imaging with predetermined isotropic gradient delay correction. Proceedings in: the 14th Annual Meeting of International Society of Magnetic Resonance in Medicine 2006.
72. Alley MT, Glover GH, Pelc NJ. Gradient characterization using a Fourier-transform technique. *Magn Reson Med.* 1998;39(4):581-587.
73. Nakamoto Y, Osman M, Cohade C, et al. PET/CT: comparison of quantitative tracer uptake between germanium and CT transmission attenuation-corrected images. *J Nucl Med.* 2002;43(9):1137-1143.
74. Hernando D, Haldar JP, Sutton BP, Ma J, Kellman P, Liang ZP. Joint estimation of water/fat images and field inhomogeneity map. *Magn Reson Med.* 2008;59(3):571-580.
75. Berglund J, Johansson L, Ahlstrom H, Kullberg J. Three-point Dixon method enables whole-body water and fat imaging of obese subjects. *Magn Reson Med.* 2010;63(6):1659-1668.
76. Hernando D, Kellman P, Haldar JP, Liang ZP. Robust water/fat separation in the presence of large field inhomogeneities using a graph cut algorithm. *Magn Reson Med.* 2010;63(1):79-90.

Appendix: k-Space Trajectory Correction for mUTE

The k-space trajectories of the UTE and multi-echo radial acquisitions were measured and corrected in image reconstruction to reduce the effects of eddy currents on the resultant images. Our k-space trajectory mapping method is similar to that in ^{1,2}, which measures the phase accrual at each time point throughout various spatial locations to map the actual k-space trajectory traversed by the readout gradient of interest. The pulse sequence diagram of the employed k-space trajectory correction sequence is shown in Supplementary Figure S1. Spatial localization was achieved using a slice-selective RF excitation pulse followed by phase-encoding gradients in two directions for 2D imaging. Free-inductive-decay (FID) signals were subsequently acquired to measure the phase accrual caused by magnetic field inhomogeneity alone (“Gradient-Off”) and the additional phase accrual caused by the gradient structure of interest (“Gradient-On”). More specifically, the signal obtained in the “Gradient-On” acquisition at spatial location x and time t of the acquisitions can be written as:

$$S(x, t) = I(x) \cdot e^{-i(\emptyset(t))} \quad [1]$$

The phase term $\emptyset(t)$ consists of two terms:

$$\emptyset(t) = \emptyset_{B_0}(t) + \emptyset_G(t) \quad [2]$$

where $\emptyset_{B_0}(t)$ denotes the phase accrual at time t due to magnetic field inhomogeneity B_0 and $\emptyset_G(t)$ denotes the phase accrual at time t due to the execution of the gradient structure of interest. The phase contribution due to $\emptyset_{B_0}(t)$, i.e., $\emptyset_{B_0}(t) = 2\pi \cdot \Delta f_{B_0} \cdot t$, can be removed via subtraction of $\emptyset(t)$ between acquisitions with (Supplementary Figure S1a) and without (Supplementary Figure S1b) the execution of the gradient structure of interest. Then, the k-space trajectory traversed by the gradients can be estimated by further writing $\emptyset_G(t)$ as:

$$\emptyset_G(t) = x \cdot \gamma \cdot \int_{t_0}^t G(\tau) d\tau = 2\pi \cdot x \cdot k_G(t) \quad [3]$$

where γ denotes the gyromagnetic ratio, t_0 denotes the starting time of the gradient G , and $k_G(t)$ denotes the time evolution of the k-space trajectory traversed by the readout gradients of interest.

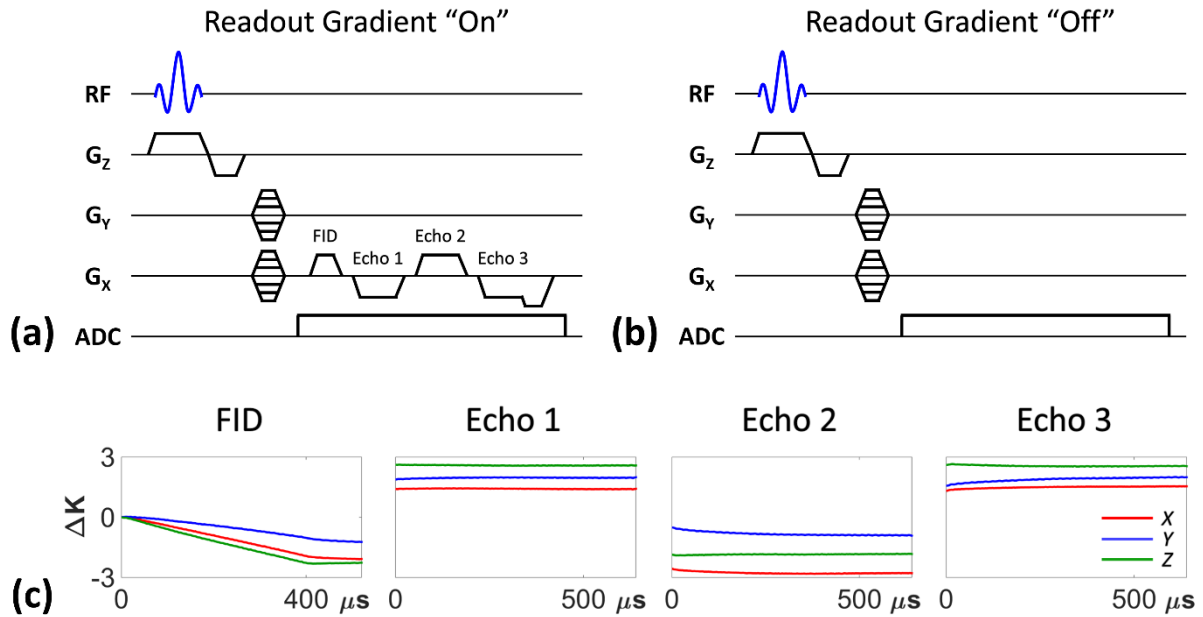
The k-space trajectory was measured for the proposed mUTE sequence by performing experiments with a water phantom on the scanners used for phantom and in vivo studies, the

whole-body 3T MR scanner (MAGNETOM Trio, Siemens Healthcare, Erlangen, Germany) and whole-body PET/MR scanner (Biograph mMR, Siemens, Erlangen, Germany), using a head coil for reception and body RF coil for transmission. The imaging parameters were: field-of-view (FOV) = $240 \times 240 \text{ mm}^2$, resolution = $1.875 \times 1.875 \text{ mm}^2$, slice thickness = 5 mm, TR/TE = 14/2.6 ms, and total scan time = 15.3 min. The TR unit with (Supplementary Figure S1a) and without (Supplementary Figure S1b) the readout gradient structure of the mUTE sequence was acquired in an alternating fashion for each of the phase-encoding gradients, and the entire acquisition was repeated for readouts along the x -, y -, and z -gradient axes. A one-time acquisition was performed from each scanner to measure the k-space trajectory for the mUTE sequence, and the measured k-space trajectory was applied for reconstruction of all subsequent acquisitions performed across several months with the mUTE sequence from the same scanner. Following the acquisition, the phase difference between each time point (i.e., $\emptyset(\Delta t_N) = \emptyset(t_N) - \emptyset(t_{N-1})$) was evaluated first with $\emptyset(t_0) = 0$ and was subsequently used to determine $\emptyset(t)$ recursively to minimize effects from phase-wrapping. Note that for the mUTE sequence, data sampling starts from the center of the k-space. The phase contribution due to $\emptyset_{B_0}(t)$ was removed by subtracting $\emptyset(t)$ between acquisitions with (Supplementary Figure S1a) and without (Supplementary Figure S1b) the readout gradients of the mUTE sequence. Subsequently, $k_G(t)$ was derived via linear fitting with least-squares method.

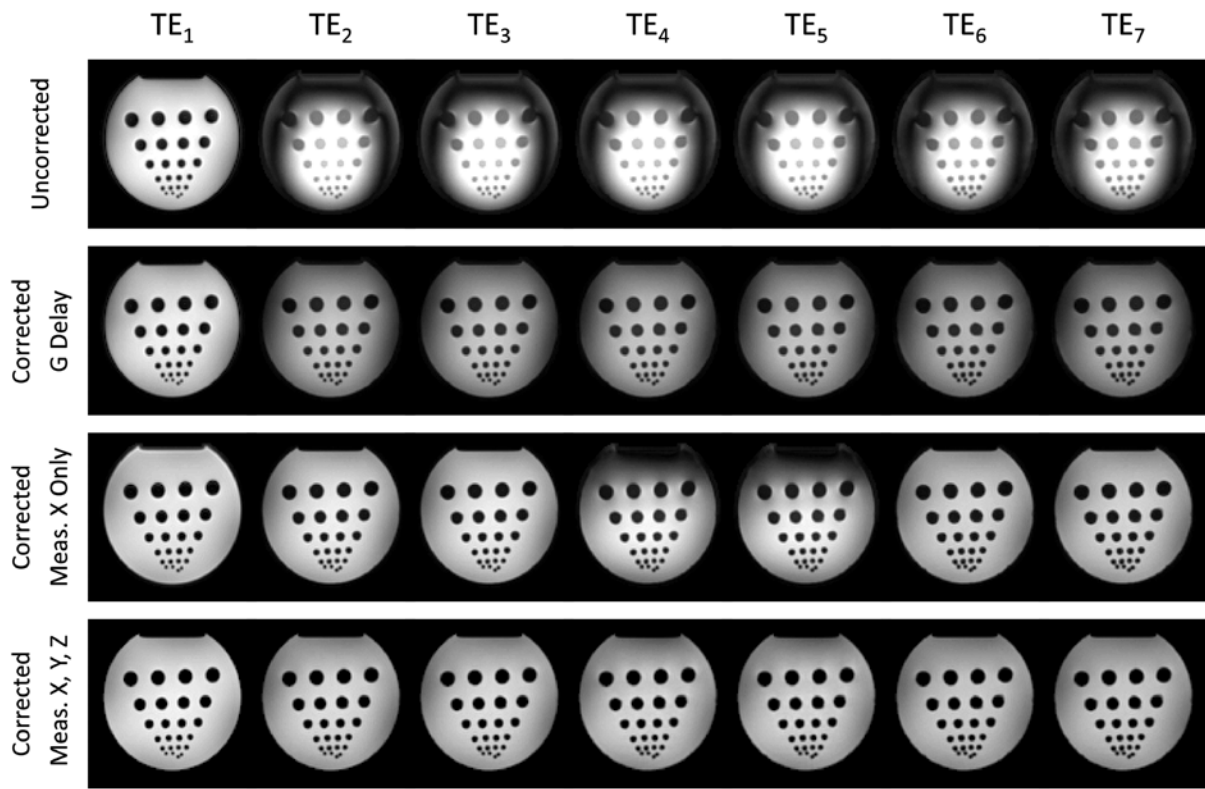
References

1. Duyn JH, Yang Y, Frank JA, van der Veen JW. Simple correction method for k-space trajectory deviations in MRI. *J Magn Reson.* 1998;132(1):150-153.
2. Alley MT, Glover GH, Pelc NJ. Gradient characterization using a Fourier-transform technique. *Magn Reson Med.* 1998;39(4):581-587.

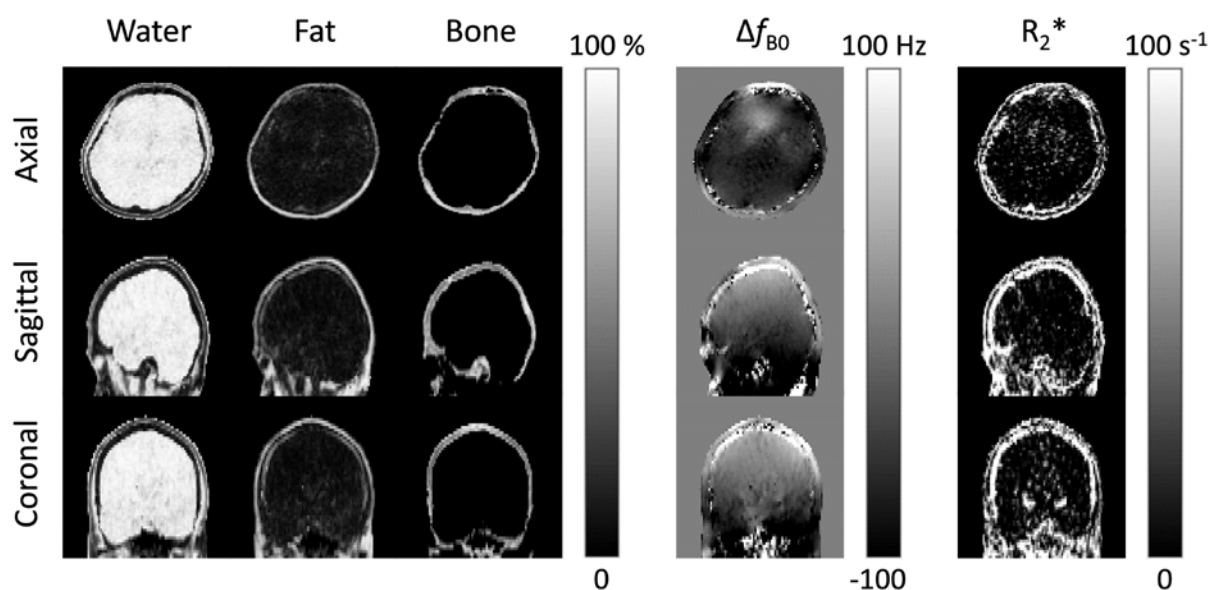
Supplementary Figures and Table



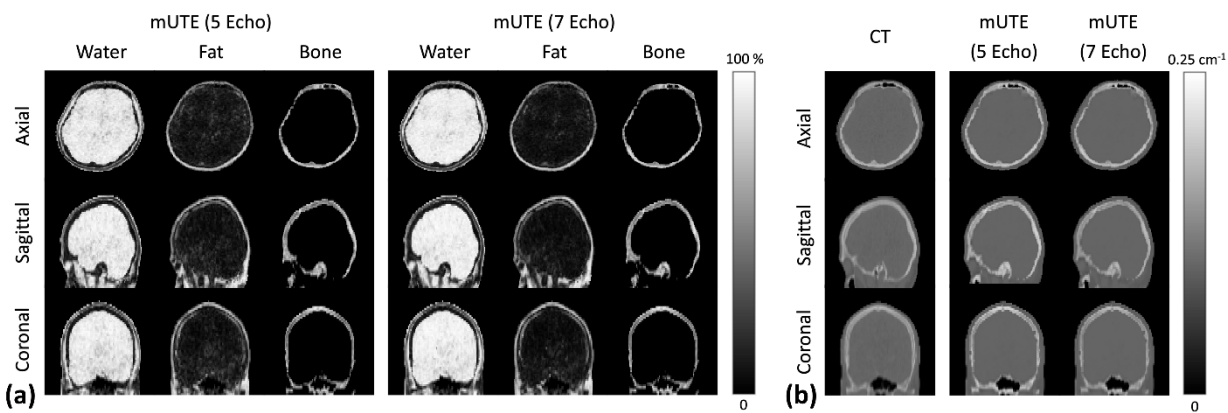
Supplementary Figure S1. The k-space trajectory mapping sequence. **a:** Pulse sequence diagram of the k-space trajectory mapping sequence with the gradient structure of interest (e.g., readout gradients in the mUTE sequence). **b:** Pulse sequence diagram of the k-space trajectory mapping sequence without the gradient structure of interest. **c:** Nominal and measured k-space trajectory of the readout gradients in the mUTE sequence from x - (red), y - (blue) and z - (green) gradient axes. Notice the difference in measurement from the different gradient axes.



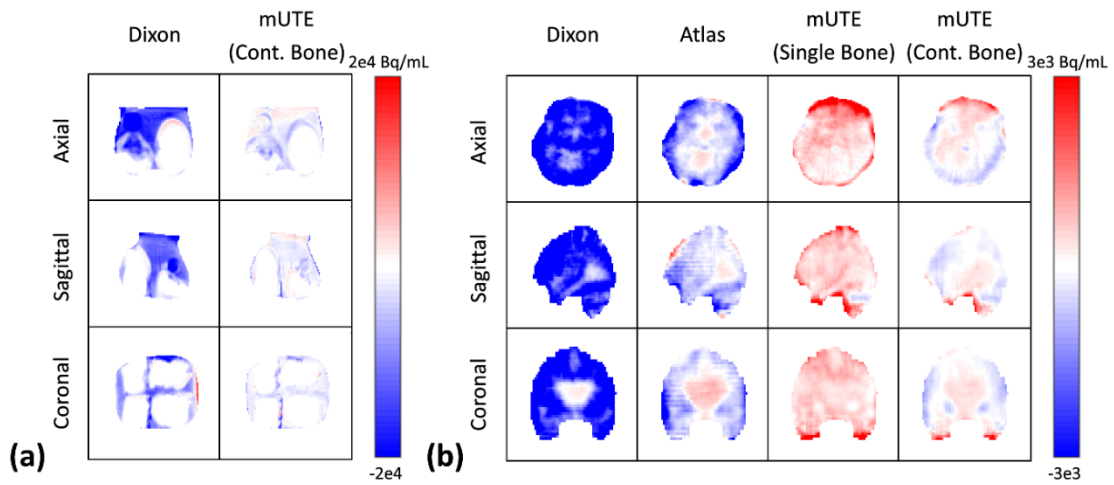
Supplementary Figure S2. Phantom experiment results of k-space trajectory correction for mUTE sequence. Images reconstructed without k-space trajectory correction and with k-space trajectory correction using gradient delay, measurements from the x -gradient axis only, and measurements from x -, y -, and z -gradient axes are shown. Notice the remaining signal loss and distortion in images when k-space trajectory was corrected using gradient delay or measurements from the x -gradient axis only. Also notice the improvement when k-space trajectory was corrected using measurements from x -, y -, and z -gradient axes.



Supplementary Figure S3. Estimation results of the proposed mUTE method (Subject #1). Estimated water, fat, and bone proton density fraction, Δf_{B0} , and R_2^* maps from the proposed mUTE method are shown.



Supplementary Figure S4. Results of quantification and LAC maps from the proposed mUTE method with different number of echoes (Subject #1). **a:** Water, fat, and bone proton density fraction maps from the proposed mUTE method using 5 and 7 echoes. **b:** LAC maps from the proposed mUTE method using 5 and 7 echoes.



Supplementary Figure S5. Results of PET percentage error maps in absolute units. **a:** PET percentage error maps from the phantom experiment. **b:** PET percentage error maps from the in vivo experiment (Subject #1).

Supplementary Table 1. Regional Mean Relative Absolute Error of Reconstructed PET Images from Subject #1

	Mean Relative Absolute Error (%)			
	Dixon	Atlas	mUTE (Single Bone)	mUTE (Cont. Bone)
Frontal	13.7 (11.7 ± 3.1)	4.8 (4.3 ± 1.9)	6.1 (4.3 ± 1.2)	2.9 (2.0 ± 0.6)
Temporal	12.1 (12.0 ± 2.7)	5.9 (5.9 ± 2.2)	8.5 (5.9 ± 1.6)	5.6 (3.9 ± 1.2)
Parietal	15.0 (12.9 ± 3.8)	3.1 (3.5 ± 2.1)	3.6 (3.8 ± 1.4)	1.0 (1.2 ± 0.4)
Occipital	13.0 (11.5 ± 3.4)	3.4 (3.8 ± 1.9)	2.2 (2.2 ± 0.7)	0.9 (1.1 ± 0.5)
Cerebellum	13.9 (13.8 ± 2.9)	7.9 (6.6 ± 2.6)	7.1 (5.5 ± 1.4)	5.5 (4.7 ± 1.4)
WM	8.9 (9.0 ± 1.7)	2.2 (2.5 ± 0.5)	2.9 (2.5 ± 0.3)	1.4 (1.2 ± 0.2)
GM	13.5 (12.0 ± 2.9)	4.6 (4.5 ± 1.6)	5.9 (4.5 ± 0.9)	3.1 (2.3 ± 0.5)

^a Group result shown in parenthesis (mean ± standard deviation)